









Tracing spatial confinement in semiconductor quantum dots by high-order harmonic generation

H. N. Gopalakrishna ^{1,2}, R. Baruah,^{3,4} C. Hünecke ⁴, V. Korolev,¹ M. Thümmler ⁴, A. Croy ⁴, M. Richter,⁴ F. Yahyaei ⁵, R. Hollinger,¹ V. Shumakova,⁶ I. Uschmann,^{1,2} H. Marschner,^{1,2} M. Zürich,^{1,7} C. Reichardt,³ A. Undisz,⁸ J. Dellith,³ A. Pugžlys,⁶ A. Baltuška,⁶ C. Spielmann,^{1,2,9} U. Peschel ^{5,9}, S. Gräfe,^{4,9,10} M. Wächtler ^{3,4,9,*} and D. Kartashov ^{1,9,†}

¹Institute of Optics and Quantum Electronics, Friedrich-Schiller University Jena, Max-Wien-Platz 1, 07743 Jena, Germany

²Helmholtz-Institut Jena, Helmholtzweg 4, 07743 Jena, Germany

³Leibniz Institute of Photonic Technology, Albert-Einstein-Straße 9, 07745 Jena, Germany

⁴Institute of Physical Chemistry, Friedrich Schiller University Jena, Helmholtzweg 4, 07743 Jena, Germany

⁵Institute of Condensed Matter Theory and Solid-State Optics, Friedrich Schiller University Jena, Fröbelstieg 1, 07743 Jena, Germany

⁶Institute for Photonics, Vienna University of Technology, Gußhausstraße, 25-29, 1040 Vienna, Austria

⁷Department of Chemistry, University of California, Berkeley, Berkeley, California 94720, USA

and Materials Sciences Division, Lawrence Berkeley National Laboratory, Berkeley, California 94720, USA

⁸Institute of Materials Science and Engineering, Chemnitz University of Technology, Erfenschlager Straße 73, 09125 Chemnitz, Germany and Otto Schott Institute of Materials Research, Friedrich Schiller University Jena, Löbdergraben 32, 07743 Jena, Germany

⁹Abbe Center of Photonics, Albert-Einstein-Straße 6, 07745 Jena, Germany

¹⁰Fraunhofer Institute for Applied Optics and Precision Engineering, Albert-Einstein-Straße 7, 07745 Jena, Germany



(Received 6 September 2022; accepted 16 December 2022; published 17 February 2023; corrected 9 March 2023)

We report here on results of systematic experimental-theoretical investigation of high-order harmonic generation (HHG) in layers of CdSe semiconductor quantum dots of different sizes and a reference bulk CdSe thin film. We observe a strong decrease in the efficiency, up to complete suppression of HHG with energies of quanta above the band gap for the smallest dots, whereas the intensity of below band gap harmonics remains weakly affected by the dot size. In addition, it is observed that the suppression of the above gap harmonics is enhanced with increasing the driving wavelength. These systematic investigations allow us to develop a simple physical picture explaining the observed suppression of the highest harmonics: the discretization of electronic energy levels seems to be not the predominant contribution to the observed suppression but rather the confined dot size itself, causing field-driven electrons to scatter off the dot's walls. The reduction in the dot size below the classical electron oscillatory radius and the corresponding scattering limits the maximum acceleration by the laser field. Moreover, this scattering leads to a chaotization of motion, causing dephasing and a loss of coherence, therefore suppressing the efficiency of the emission of highest-order harmonics. Our results demonstrate a regime of intense laser-nanoscale solid interaction, intermediate between the bulk and single-molecule response, and are crucial for nanophotonic platforms aiming at control over high-order harmonic properties and efficiency.

DOI: [10.1103/PhysRevResearch.5.013128](https://doi.org/10.1103/PhysRevResearch.5.013128)

I. INTRODUCTION

After the first theoretical prediction [1] and experimental demonstration [2], high-order harmonic generation (HHG) in bulk solids became a rapidly growing research field in ultrafast strong-field physics. Numerous experiments have shown that, due to the nonlocal nature of the strong-field-driven nonlinearity of the carrier's quantum dynamics, HHG in crystalline

solids has great potential as an ultrafast spectroscopy probe, sensitive to crystal symmetry and structure [3,4], electronic band structure [5–7], etc., with subcycle temporal and picometer spatial resolution [8,9].

The physics of HHG in bulk solids is well understood. After electron excitation from the valence to the conduction band by the strong laser field, high-order harmonics are generated by two mechanisms: the intraband electron-hole currents in the conduction and valence bands (nonlinear Bloch current, a consequence of the nonparabolicity of the bands), and nonlinear polarization between the field-driven electrons and holes during their phase-locked motion in the corresponding bands. The first mechanism contributes mostly to harmonics with energies of quanta below the band gap, whereas the second mechanism dominates the emission spectrum above the band gap and ultimately requires coherent electron-hole motion [10].

The question that we address here is “How is the HHG process impacted by confinement, when the crystallite's size

*Present address: Department of Chemistry and Research Center OPTIMAS, RPTU Kaiserslautern-Landau, Erwin-Schrödinger-Straße 52, 67663 Kaiserslautern, Germany

†daniil.kartashov@uni-jena.de

Published by the American Physical Society under the terms of the Creative Commons Attribution 4.0 International license. Further distribution of this work must maintain attribution to the author(s) and the published article's title, journal citation, and DOI.

is reduced down to the nanoscale?” Spatial confinement leads to a breakdown of basic concepts used in solid state physics and has multiple effects on the carrier dynamics in solids. A spatial extent of the system of only a few unit cells leads (a) to a discretized energy structure, putting under question the concept of bands itself; (b) to effective masses becoming less well defined, because they depend not only on the band, but also on the actual position in the coordinate space within the nanocrystallite; (c) to a reduction of the relative contribution of the volume towards an increased role of surface states; and (d) to scattering from the potential barrier at the crystallite’s surface (“off-the-wall” scattering) when the crystallite’s size is comparable to or less than the amplitude of the oscillatory motion of the electron wave packet, excited and driven by the laser field. At the same time, nanocrystallites, still composed of hundreds or even thousands of atoms, are still far from the atomic or molecular scales. Therefore, the question is “How can we trace the impact of confinement on HHG and which mechanisms contribute to HHG most in strongly confined systems?”

Very recently, the first experimental results on HHG in CdSe quantum dots of different sizes and a fixed $3.5\ \mu\text{m}$ laser wavelength have been reported [11]. In these experiments, an abrupt drop in the harmonic intensity for quantum dots with a diameter less than $3\ \text{nm}$ has been observed. It has been suggested that this effect originates from the discrete electronic energy structure in the conduction band of small dots that leads to a suppression of intraband transitions and, by that, a suppression of HHG [11]. However, several aspects in these results remain puzzling: for example, calculations of the energy level structure for the dots with sizes up to $2\ \text{nm}$ show that the energy spacing between the lowest unoccupied levels is still much smaller than the energy of the laser quanta used in the experiments in [11]. Therefore, it is not clear why discretization would lead to a suppression of intraband harmonics. To shed light on this phenomenon, we present here a more detailed experimental and theoretical study in a broad parameter range.

Here, we experimentally investigate HHG in layers of CdSe semiconductor quantum dots (QDs) of different diameter as a function of the laser intensity, ellipticity, and wavelength. We likewise see that above band gap harmonics show an abrupt and pronounced drop in intensity for dot diameters below $3\ \text{nm}$, in agreement with [11]. Moreover, we demonstrate that this effect becomes especially pronounced for longer laser wavelengths. However, harmonics with energies near the band gap energy, that have a comparable contribution of intraband and interband generation mechanisms [10], are not sensitive to change in the dot diameter. Also, we investigate the dependence of harmonic yield on the pumping intensity and ellipticity as a function of the dot’s diameter. We show that, whereas the ellipticity dependence is almost the same in the reference bulk and dots of all sizes, the intensity dependence demonstrates a gradual increase in the nonlinearity of HHG with reducing the dot’s size.

Our experimental results, supported by numerical simulations, suggest that, despite the visible discretization of the electronic energy structure, this seems to play a minor role, as the energy spacing is still much smaller than the driving frequency for all cases. Instead, the major effect on HHG

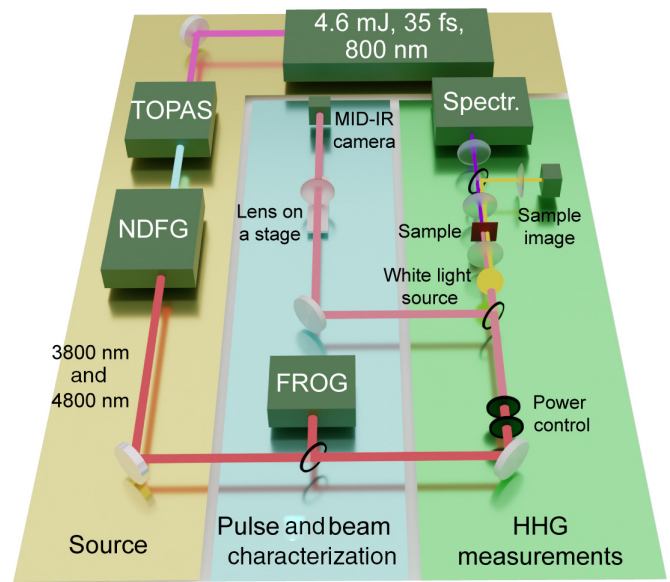


FIG. 1. Experimental setup: NDFG: noncollinear difference frequency generation module, providing tunable mid-IR pulses by DFG between the signal and idler waves; FROG: frequency-resolved optical gating apparatus for pulse characterization. The lens on the stage with a mid-IR CCD camera was used for focus beam profile characterization. A white-light source with a $50\times$ removable infinity-corrected objective (not shown), a lens, and a CCD camera were used as an imaging system for the on-site sample diagnostic.

efficiency can be explained within a simple classical picture: for dot sizes below the classical oscillatory radius of the electron in the laser field, scattering at the dots’ walls leads to an out-of-phase dynamics relative to the laser optical cycles, and, thus, to a reduced acceleration. This, in turn, prevents the generation of the highest harmonics.

The manuscript is organized as follows. The experimental setup, sample design, and characterization are described in Sec. II and the Appendix. The results of experimental measurements are discussed in Sec. III. The results of numerical simulations are presented in Sec. IV, followed by discussions and conclusions.

II. EXPERIMENTAL SETUP AND SAMPLE CHARACTERIZATION

The experiments were carried out using a femtosecond optical parametric amplifier system (Light Conversion TOPAS Prime) pumped by a $35\ \text{fs}$ laser source at $0.8\ \mu\text{m}$ wavelength (Coherent, Astrella), followed by a difference frequency generation stage, providing $70\text{--}100\ \text{fs}$ pulses tunable in the spectral range $3\text{--}16\ \mu\text{m}$. The temporal shape of the pulses was characterized via frequency-resolved optical gating (FROG) based on second harmonic generation (SHG), whereas the focal intensity distribution was characterized using a mid-IR CCD camera. The experimental setup is depicted in Fig. 1. The mid-IR laser beam was focused by a $f = 75\ \text{mm}$ lens at normal incidence onto a quantum dot layer, deposited on a substrate, in a spot of $85\ \mu\text{m}$ diameter (e^{-2} intensity level). The high-order harmonic radiation transmitted through the substrate was collimated by a CaF_2 lens and then focused on the entrance slit of a spectrometer (Kymera-328i) equipped

TABLE I. Characteristics of quantum dot layers.

Dot diameter from peak position (nm)	Dot diameter d from TEM (nm)	Band gap from Tauc plot (eV)	Band gap from emission peak (eV)	Layer thickness (μm)
2.2	2.6	2.48	2.48	2.4
3	3.4	2.18	2.21	3.8
4	4.2	2.05	2.08	4.5
8.2	7.7 ^a	1.89	1.89	2.8

^aThe 8.2 nm QDs are not exactly spherical and show an aspect ratio of long and short axes of 1.7:1.

by a cooled CCD camera as a detector. The spectra were measured in the spectral range 200–1100 nm limited by the spectrometer and the detector. We also employed on-site microscopy consisting of a white light source and a 50 \times microscope objective for optical diagnostics of the quantum dot layers before and after interaction with laser pulses. The microscope also allowed alignment of the HHG measurements in the vicinity of a marked area of the layer, thoroughly characterized with different diagnostic methods as described in what follows.

Colloidal CdSe quantum dots (QDs) were synthesized following established protocols via the hot injection method (for details see the Appendix) [12,13]. The surface of the QDs was covered by trioctylphosphine oxide (TOPO) which renders the QDs dispersible in nonpolar solvents, e.g., toluene. By variation of injection temperature and growth time, the size of the QDs was controlled and varied in the range between 2 and 9 nm. As expected, due to quantum confinement, the position of the excitonic transitions in the absorption and

photoluminescence spectra of the particles shift in dependence on size (see the Appendix, Figs. 13 and 14) [14]. The band gap was determined from a Tauc plot [15] and the position of the band gap photoluminescence peak. Both methods resulted in similar values (Table I). The size of the nanocrystals was determined from the spectral position of the first excitonic transition in the absorption spectra by the method described in [16] and compared to the results obtained from transmission electron microscopy (TEM) images (see Fig. 2 and the Appendix). A typical example of the statistical variations of the dots' diameter d is shown in Fig. 2(b), suggesting that full width at half maximum (FWHM) spread of the size is within 10% (for a documentation of the size distribution analysis for all samples, see the Appendix). The crystal structure was determined using x-ray diffraction (XRD) to be wurtzite (see the Appendix, Figs. 15 and 16). Note that all quantum dots employed in our experiments satisfy strong confinement criteria, meaning that the dots' diameter is smaller than exciton size in the bulk, which for CdSe is roughly 11 nm [17].

QDs dispersed in toluene were drop casted on a 500 μm thick sapphire substrate to form a thin well-ordered QD layer after solvent evaporation [Fig. 2(c)]. We targeted a layer thickness in the μm range as was confirmed by atomic force microscopy (AFM) (Table I and the Appendix). The photoluminescence peak positions determined for QD layers deposited on sapphire are identical to the spectra in solution (see the Appendix, Fig. 13); i.e., no changes in spectral position of PL peaks are observed. This confirms that there is no significant electronic interaction between the neighboring QDs after deposition, and the QDs can be regarded as isolated particles due to the presence of bulky TOPO ligand. Thus, the dots in the layers can be considered as independent emitters of high-order harmonics.

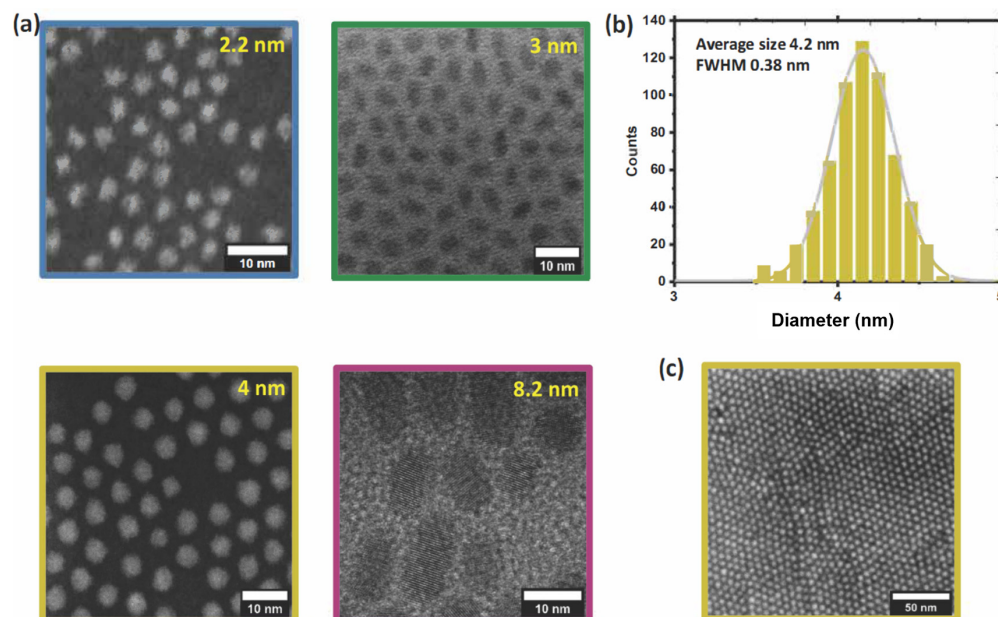


FIG. 2. (a) TEM images of quantum dots of different sizes used in this investigation. Acquisition was either carried out in scanning TEM mode using a high-angle annular detector or in TEM bright-field mode. (b) Statistical size distribution for 4 nm QDs. The analysis of the TEM images results in a mean diameter of 4.2 nm, which is in good agreement with the diameter of 4 nm determined from the position of the first excitonic transition in the absorption spectra. (c) SEM image of a layer of 4.2 nm dots deposited on a Si substrate.

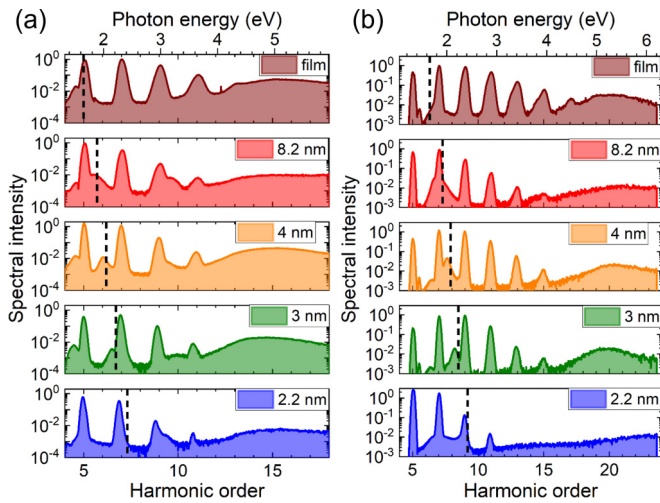


FIG. 3. Measured HHG spectra in different size QDs for (a) 3.72 μm and (b) 4.74 μm laser wavelength at a fixed intensity. The dashed line marks the band gap determined from photoemission/photoabsorption measurements.

Finally, as a reference bulk sample, we prepared a 140 nm thick polycrystalline CdSe film consisting of randomly oriented wurtzite crystallites with a diameter of 52 nm and a band gap of 1.64 eV. The film was grown on a sapphire substrate by the chemical bath deposition method [18] with subsequent vacuum annealing (for a detailed description see the Appendix).

III. EXPERIMENTAL RESULTS

The spectra were measured by irradiating quantum dots of different size with 100 fs laser pulses at a fixed laser intensity of 1.2 TW cm^{-2} , at two different wavelengths 3.72 and 4.74 μm , and are shown in Figs. 3(a) and 3(b). All spectra are corrected for the spectrometer sensitivity and acquisition time. Thus, the spectra for a fixed laser wavelength λ but different dot size can be directly compared. For both laser wavelengths, we observe significantly faster decay in amplitudes of harmonics with increasing harmonic order in quantum dots in comparison to the reference bulk film. Moreover, we observe an abrupt drop in the intensity of harmonics with energies of quanta above the band gap for dots with a diameter below $d = 3 \text{ nm}$, in agreement with the results in [11].

This effect is especially pronounced for the longer $\lambda = 4.74 \mu\text{m}$ wavelength, where essentially all harmonics above the band gap are strongly suppressed. At the same time, the efficiency of generation of the below and near the band gap harmonics (fifth and seventh for $\lambda = 3.72 \mu\text{m}$ and fifth to ninth for $\lambda = 4.74 \mu\text{m}$) remains almost unaffected by the dot's diameter.

We further investigated the dependence of the harmonic yields on the laser intensity for both wavelengths. We found that, in the range of laser intensities $0.4\text{--}1 \text{ TW cm}^{-2}$ used in the experiments, the intensity dependence of the yield for the individual harmonics can be very well fitted in a double logarithmic scale by a linear function (Fig. 4). The slope of the corresponding linear fit, i.e., the power index, as a function of the harmonic's order and different dot sizes is shown in

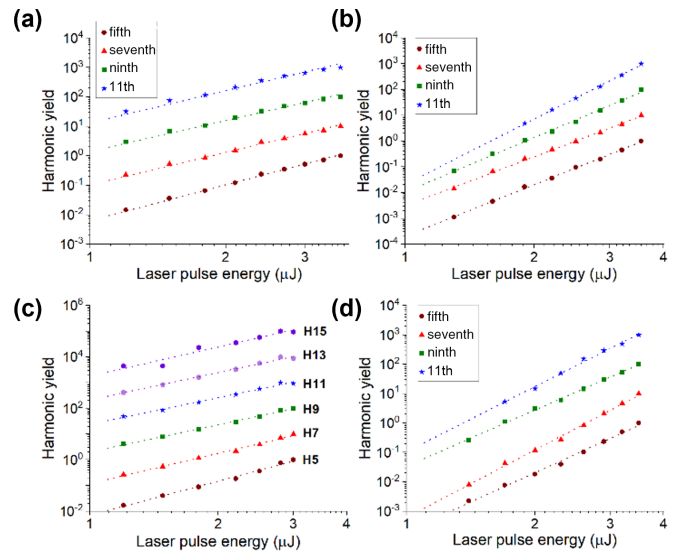


FIG. 4. Intensity dependence of the harmonic's yield for the 3.72 μm laser wavelength: (a) for the 4.4 nm size QDs and (b) 2.2 nm size QDs. Intensity dependence of the harmonic's yield for the 4.74 μm laser wavelength: (c) for the 4.4 nm size QDs and (d) 2.2 nm size QDs.

Fig. 5. For the film and large diameter dots, the power index is noticeably lower than the harmonic order, confirming the nonperturbative character of the nonlinearity. Also, the power index slightly decreases or remains approximately constant as a function of harmonic order (for a fixed dot diameter). However, for all harmonic orders the power index is higher for smaller QDs. Moreover, for the smallest QD with $d = 2.2 \text{ nm}$ the power index for the below band gap harmonics (fifth for $\lambda = 3.75 \mu\text{m}$ and fifth and seventh for $\lambda = 4.74 \mu\text{m}$) is even higher than the corresponding harmonic order. This is unexpected, because one would expect that restriction in the amplitude of the electron wave packet motion within the nanocrystal should lead to a more like perturbative character of nonlinearities; i.e., the power index should remain below or be close to the harmonic order.

Finally, we measured the polarization dependence of HHG in the reference polycrystalline film and quantum dots of different sizes when changing the laser polarization from linear to circular. The polarization dependence of harmonic yield was measured for both 3.75 and 4.74 μm laser wavelengths

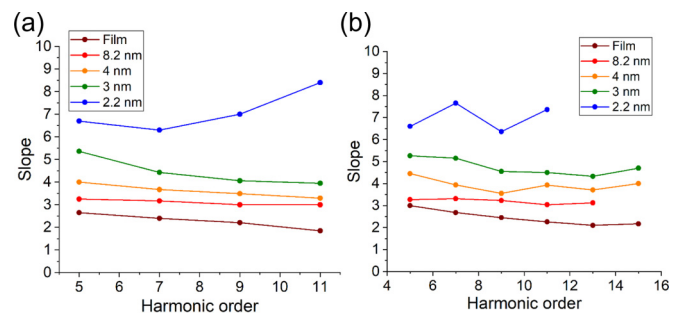


FIG. 5. The slope of the laser intensity dependence of the harmonic's yield as a function of harmonic order in the range of laser intensities $0.4\text{--}1 \text{ TW cm}^{-2}$ for (a) 3.75 μm and (b) 4.74 μm laser wavelength

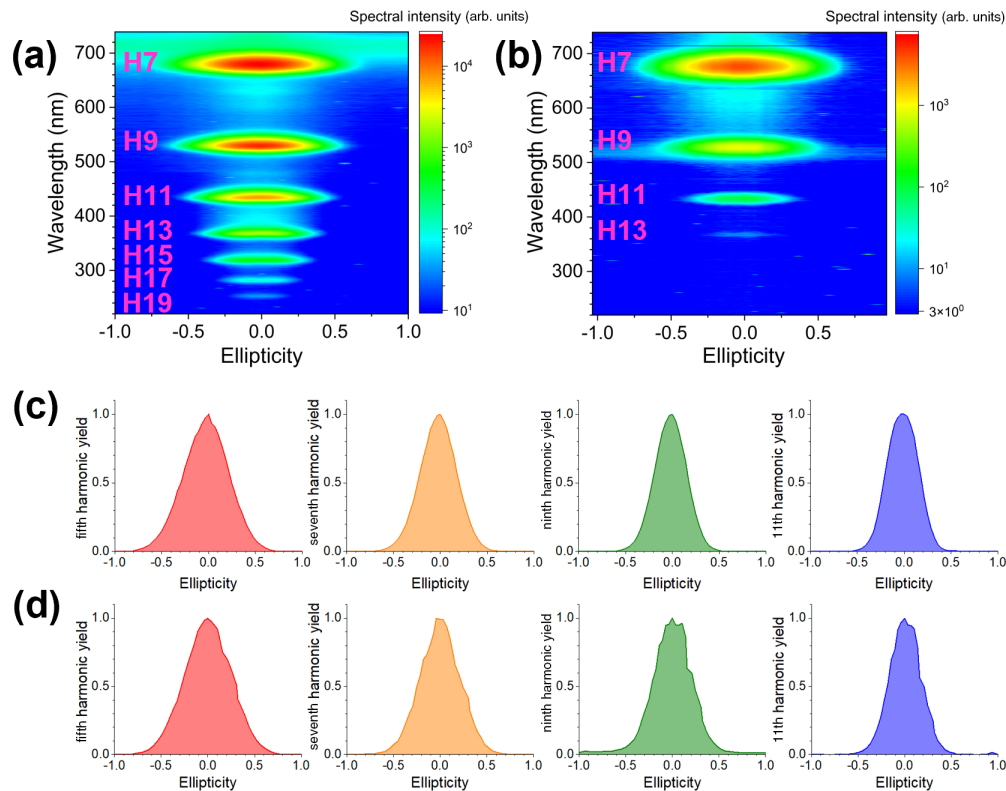


FIG. 6. Ellipticity dependence of the harmonic's yield. (a) The spectrogram for the reference film and (b) the spectrogram for 2.2 nm QDs. Note the logarithmic scale of the spectral intensity. Spectrally integrated harmonic yield for (c) the reference film and (d) 2.2 nm size QDs. The laser wavelength is 4.74 μm .

and fixed laser intensity 0.5 TW cm^{-2} . The intensity value was chosen to avoid sample degradation during the data acquisition. Laser polarization was controlled by a broadband achromatic quarter-wave plate (B-Halle), automatically rotated with a step size of 1° . HHG spectrum was measured for each wave-plate angle, forming a spectrogram that is shown in Figs. 6(a) and 6(b). The spectrum of each individual harmonic was integrated then in the frequency domain in the range $[2n, 2n + 2]$ where n is the harmonic order, and the corresponding integral value is defined as the yield. The normalized dependence of the yield for individual harmonics as a function of the ellipticity in the laser polarization is shown in Figs. 6(c) and 6(d) for the case of the reference film and 2.2 nm size QDs. The width of these dependencies is defined at half maximum level [full width at half maximum (FWHM)] and the dependence of this width on the laser polarization is shown in Fig. 7. The spectrograms and integral yields for other samples, used in the experiments, look similar to the examples in Fig. 6. The qualitative behavior of the FWHM in the ellipticity dependence as a function of the harmonic's order is the same in the film and all dots, dropping for below-near band gap harmonics and then saturating or even slightly increasing for harmonics above the ninth. This slight increase in the width of the ellipticity dependence might be due to the random orientation of crystallites in the film and dots layers. It has previously been shown experimentally and theoretically that ellipticity dependence of HHG in solids is more complicated than in gases, and that the efficiency of higher-order harmonic generation might be increased depending on the orientation of the crystal symmetry axes relative to the polarization ellipse

[19], i.e., can have maximum at a certain ellipticity. Further, we observe similar behavior of the ellipticity dependence for all dots and the bulk, suggesting that the mechanism of HHG is the same in all these samples.

Our main experimental observations can be summarized as follows: (1) The intensity of the above band gap harmonics drops abruptly when the dot diameter d is reduced below 3 nm, whereas below and near band gap harmonics remain largely unaffected. (2) the power index in the dependence of the harmonic's yield on the laser intensity gradually increases with reduction in the dot size but its value is weakly dependent on the harmonic's order. For the smallest $d = 2.2$ nm dots the power index for below band gap harmonics exceeds the corresponding harmonic order. (3) The bulk semiconductor and QDs of all sizes show a very similar

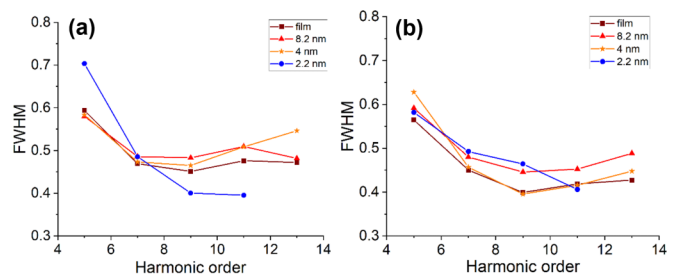


FIG. 7. FWHM of ellipticity dependence in HHG for (a) 3.75 μm and (b) 4.74 μm laser wavelength and different dot diameters. The laser intensity is fixed at 0.5 TW cm^{-2} .

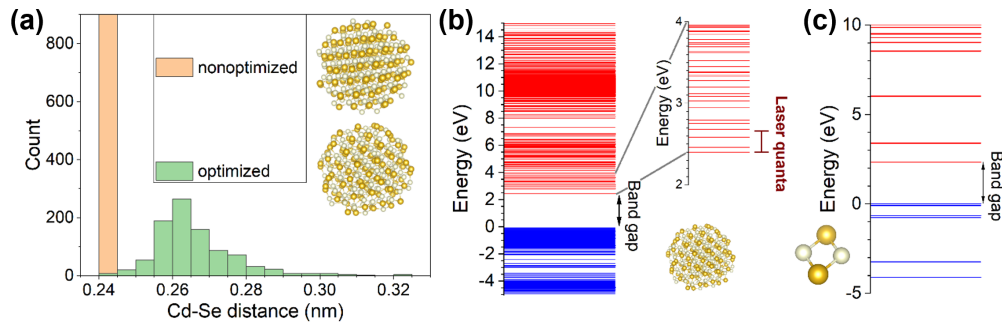


FIG. 8. (a) Visual representation of 272-atom $\text{Cd}_{136}\text{Se}_{136}$ quantum dot (diameter 2.16 nm) with spatial structure as it would be as a cut from bulk (upper image) and the energetically optimized structure (lower image). The histograms show the distribution of interatomic distances between Cd and Se atoms; (b) electronic energy structure of $\text{Cd}_{136}\text{Se}_{136}$ quantum dot with optimized geometry and (c) Cd_2Se_2 molecule. The blue levels are fully occupied and form in the bulk valence band(s), whereas the red levels show unoccupied states and form conduction bands. The inset in (b) shows a close-up of the bottom of the conduction band. The bar shows the scale of the laser quanta energy 0.26 eV, corresponding to the $4.72 \mu\text{m}$ wavelength.

dependence of the harmonic yield on the laser polarization ellipticity.

IV. NUMERICAL SIMULATIONS

We first calculated the static spatial and electronic structure of the quantum dots. Due to the system's size, we calculated the electronic energy structure using the tight-binding model GFN1-xTB as implemented in the xTB program package [20]. The structure and energies for different sizes of quantum dots, ranging from small Cd_2Se_2 molecular-type units up to CdSe clusters with diameters of $d \approx 4 \text{ nm}$ were calculated. The corresponding results for the $d \approx 2.2 \text{ nm}$ dot ($\text{Cd}_{136}\text{Se}_{136}$) and Cd_2Se_2 molecule, equivalent to one unit cell in the bulk crystal, are shown in Fig. 8. First, it should be noted that the spatial structure of small quantum dots is different from the crystalline structure in the bulk. In Fig. 8(a) the arrangements of Cd (white spheres) and Se (yellow spheres) atoms in a 2.2 nm size dot is shown for the case as it would be in a cut from a wurtzite bulk crystal and for the case of energetically optimized geometry. The crystal structure is more compact than the optimized dot structure, as shown in histograms of interatomic distances between Cd and Se atoms for both structures in Fig. 8(a). The electronic energy structure for the optimized geometry 2.2 nm dot is shown in Fig. 8(b). As follows from Fig. 8(b), with changing the size, not only the precise value of the band gap [or, for the molecule, highest occupied molecular orbital–lowest unoccupied molecular orbital (HOMO-LUMO) gap, Fig. 8(c)] changes. Also, the energy gap between the individual occupied and unoccupied states changes substantially, as expected: the larger the dot, the closer the energy levels (of similar electronic character) become, forming, in the limit of an infinite, periodic system, a band. For the dots of $d \approx 2.2 \text{ nm}$ diameter, the discrete structure of electronic states is well visible [Fig. 8(b)]. However, the energy level spacing is still substantially smaller than the energy of the laser photons ($\hbar\omega = 0.26 \text{ eV}$ for $\lambda = 4.74 \mu\text{m}$ laser); see inset in Fig. 8(b). This suggests that the discretization of the electronic energy structure does not play a significant role in the suppression of harmonic radiation even for the smallest 2.2 nm diameter dots used in the experiments.

To simulate HHG in the bulk reference and quantum dots, we first employed an *ab initio* approach based on real-time, real-space time-dependent density functional calculations (rtTDDFT) using the OCTOPUS code [21] with local density approximation (LDA) in the form of Slater-exchange, modified Perdew-Zunger-correlation functionals [22] and LDA-based pseudopotentials from [23].

For the bulk calculations, periodic boundary conditions were used whose k space was discretized by $32 \times 32 \times 20 k$ points. The laser field polarization was oriented along the Γ - K direction, and no rotational averaging was applied because of the very high computational costs of the simulations. The bulk structure had wurtzite CdSe symmetry with lattice parameters $a = 4.394 \text{ \AA}$, $b = 7.171 \text{ \AA}$ [24].

Calculations with CdSe particles of different size ranging from four atoms, over 1 nm particle size (16 atoms) to 1.5 nm particle size (64 atoms)—the largest size that could be simulated within a reasonable timescale [for 1.5 nm particle requires $>270 \text{ kCPU}$ hours on a supercomputer cluster for one single set of laser parameters. For the bulk, a single calculation (without orientation averaging) requires $>100 \text{ kCPU}$ hours]—were performed. For these calculations, energy-optimized geometries of dots were used. The radii of the spherical real-space grid were 25, 30, and 35 bohrs (depending on particle size), including 5 bohrs of complex absorbing potential at the edge of the simulation box to avoid wave function reflections.

The linearly polarized laser pulse was defined by a \sin^2 envelope with an amplitude of 1.8×10^{-3} in atomic units, corresponding to an intensity of $1.2 \times 10^{11} \text{ W cm}^{-2}$, frequency 0.012 a.u. ($3.8 \mu\text{m}$ wavelength) and a few-cycle duration, limited by the calculation costs [see Fig. 9(a)]. The HHG spectrum was calculated by the Fourier transform of the x component (along the laser polarization) of the dipole acceleration. The spectra for the bulk and the 64-atom QD are shown in Fig. 9(b). Clear suppression of harmonics above the third is observed in the dot in comparison to the bulk material. We have to note here that the calculation results for the bulk may not have fully converged. The reason is that, for good convergence in rt-TDDFT calculations by OCTOPUS, a mesh consisting of at least 70 grid points along each direction in k space is recommended [25]. This resolution

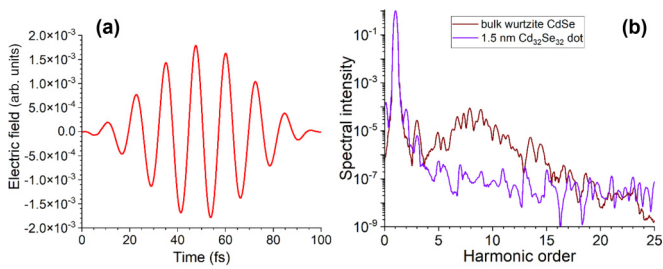


FIG. 9. (a) Modeled electric field (in atomic units) in the laser pulse. (b) HHG spectra for the bulk (wine curve) and 64 atoms QD (violet curve). The spectra are normalized to their maxima.

for time-dependent simulations is currently not feasible for the wurtzite bulk CdSe structure. In general, such simulations are computationally extremely demanding and costly and their difficulty sharply increases with increasing the laser wavelength. *Ab initio* calculations for HHG in solids were reported so far either for few-optical-cycle near-IR laser pulses [26] or mid-IR laser pulses but in highly symmetric materials such as crystalline Si [7], using one of the world's top large computer clusters. We compared the results of HHG spectra calculations, obtained with the highest possible resolution $32 \times 32 \times 20$ k -point grid, with calculations employing a $16 \times 16 \times 10$ grid and found little difference in harmonic intensities for harmonics up to the 15th order. Therefore, that the—two to three orders of magnitude difference in harmonic intensities between the bulk and QD spectra shown in Fig. 9 correctly reflects the effect of strong HHG suppression in dots in comparison to the bulk. Thus, these calculations confirm a strong suppression of harmonic intensities for $d \approx 1.5$ nm diameter dots in comparison to the bulk, but do not allow a systematic study of dots with varying diameters.

To develop a different model, we refer to the experimentally observed difference in the behavior of below and above band gap harmonics with reducing the dot's size. We remind the reader that the band gap energy separates two mechanisms of harmonic generation—the nonlinear intraband current dominating harmonics below the band gap and the interband recombination/polarization that generates harmonics above the band gap [10]. As both intra- and interband currents are proportional to the carrier density, the observed weak sensitivity of near-band-gap harmonics to the dot's diameter and sharp drop for above band gap harmonics for small dots suggest that this difference does not originate from a strongly reduced excitation rate for small dots, as has been suggested in [11] and explained by the discretization of the electronic energy structure. Instead, another mechanism, selectively affecting the carrier acceleration by the laser field and recombination, should be at play. Also, the qualitatively and quantitatively nearly identical dependence of the harmonic yield on the ellipticity of the laser polarization, suggests that the mechanisms of HHG should be the same for the film and QDs of all sizes.

Therefore, we applied a commonly used simple model to analyze the origin of the experimentally observed confinement effects in HHG. Briefly, we numerically solve the one-dimensional time-dependent Schrödinger equation (TDSE) for a single active electron in a box of finite size to investigate

the laser-field-driven quantum dynamics of electrons in the dots. The dot is modeled by the potential

$$V(x) = \begin{cases} -V_0, & |x| \leq d/2 \\ -\frac{q}{\sqrt{(|x-d/2|^2 + \frac{d^2}{V_0^2})}}, & |x| > d/2. \end{cases}$$

Here, the amplitude V_0 defines the specific work of the dot, the wall charge q determines the steepness of the wall potential, and d is the dot diameter. In the simulations, we choose $V_0 = 0.24$ a.u. (6.6 eV) to mimic the work function of CdSe [27] and a wall charge $q = 1$. We note that the precise choice of the wall charge does not influence the results substantially. For the chosen parameters, the energy gap between the stationary ground and the first excited states in the dots of 2.2, 3, and 4 nm diameter is 0.154, 0.092, and 0.056 eV, correspondingly. These energies are less than the energy of quanta for the laser wavelengths 3.75 and 4.75 μm used in simulations. Therefore, the particle in the box model has the following important differences from calculations based on the bulk band structure: (1) As it is a single-particle model, many-body contributions (such as electron-hole dynamics, etc.) are intrinsically not accounted for. (2) Despite the very dense energy spacing in the model, there are neither quantitatively correct valence energy levels, nor a proper energy gap. In our model, immediately with the onset of the laser field, an electron wave packet is launched and starts to move across the box (“inside the quantum dot,” mimicking the current contribution to HHG). (3) The electron wave packet driven inside the potential well may bounce off the dots' walls. This leads to dynamics which is not periodic with respect to the laser field; therefore, the emitted spectrum does not feature pronounced harmonics but rather a continuum structure. (4) As the potential inside the well is flat, harmonics are generated only when an electron wave packet is accelerated near the walls, in the region where the dipole acceleration $\ddot{d} = \int_{-\infty}^{\infty} |\Psi|^2 \frac{\partial V}{\partial x} dx$ is nonzero. We note parenthetically that a model potential which includes an atomiclike structure does not change the results noticeably. We therefore restrict ourselves to the simple model to extract the phenomena more clearly. Despite its shortcomings, our simple model still gives us an idea about the motion of a laser-driven charged particle under the influence of confinement. In fact, the main features of particle dynamics, as will be shown later, can even be well described classically.

The calculated spectra of the dipole acceleration for the laser intensity 0.3 TW cm^{-2} , pulse duration 75 fs FWHM (\sin^2 envelope), laser wavelengths $\lambda = 3.75$ and 4.75 μm , and different dot sizes are shown in Fig. 10. The results of the quantum dynamical simulations reproduce very well the experimentally observed effect of suppression of highest-order harmonics when reducing the dot's size. Also, they confirm that the harmonic suppression becomes more pronounced with increasing the laser wavelength. For the chosen parameters, ionization (expressed in terms of loss of norm of the wave functions caused by parts of the electronic wave function leaving the grid) remains negligible throughout. Therefore, we can conclude that harmonics are generated due to wavepacket dynamics within the potential well.

As mentioned above, the systems' dynamics is even well described classically. Thus, to get further insight, we

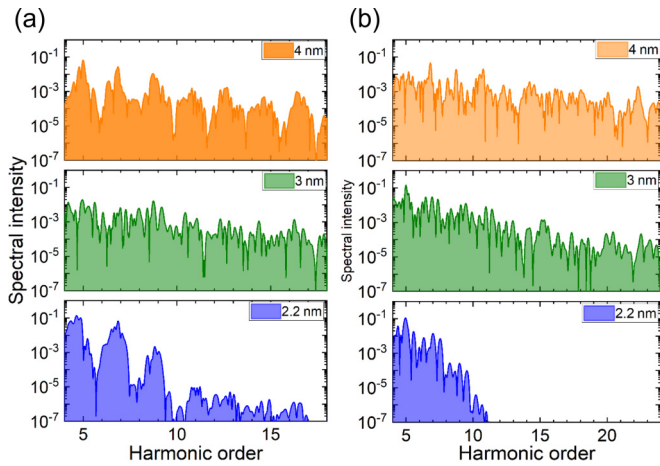


FIG. 10. Simulated dipole acceleration spectra in QDs of different sizes for (a) 3.75 μm and (b) 4.75 μm laser wavelengths. The irregular structure of the spectrum is the consequence of scattering at the walls; see in the text.

complemented the TDSE quantum calculations by a one-dimensional Monte Carlo trajectory analysis, based on 10^6 electron trajectories weighted by Wigner probability distribution over the initial coordinate and momentum distribution of the quantum mechanically calculated ground state in the model potential. To define the initial probability distribution, the quantum mechanical ground state was calculated using the imaginary time propagation [28] on a grid ranging from $-3d$ to $3d$ with 2048 spatial grid points and a time step size of $\tau = 0.2$ a.u. until the energy was converged. Afterwards, the Wigner distribution is calculated. We used rejection sampling in a uniformly sampled rectangle in the phase space to set up the initial conditions for the 10^6 trajectories. The maximum position and momentum were chosen, such that the remaining quasiprobability adds up to less than 0.01. The laser pulse was modeled as $E(t) = E_0 \sin^2(t/\tau_p) \sin \omega t$ with a pulse duration 75 fs FWHM, intensity 0.3 TW cm^{-2} , and frequencies corresponding to 3.75 or 4.75 μm wavelengths. The field within and outside the dot was calculated, using the analytical solution for the potential of a dielectric sphere exposed to a spatially homogeneous external electric field, i.e., $V = -\frac{3\epsilon_v}{\epsilon_d + 2\epsilon_v} xE(t)$, for $|x| < d/2$, and $V = -xE(t) + \frac{\epsilon_d - \epsilon_v}{\epsilon_d + 2\epsilon_v} \frac{xd^3}{|2x^3|} E(t)$ otherwise, with a vacuum permittivity of $\epsilon_v = 1$ and a dot permittivity of $\epsilon_d = 6$ [29]. The dense time propagation of all the trajectories was done using the SCIPY.INTEGRATE.LSODA function.

We used for the calculations the same laser pulse parameters as were used in TDSE calculations. In Fig. 11, the dynamics of some selected (neighboring) trajectories are displayed.

We see very clearly that for larger dots, the dynamics directly follows the laser oscillations with an oscillatory radius of $r_{\text{osc}} = E_0/\omega^2$ (in atomic units), while in smaller dots, when $d < r_{\text{osc}}$, trajectories bounce off the walls. This, in turn, has two consequences: (i) the scattering off the walls leads to a kind of chaotization of dynamics, which, in a quantum picture, would correspond to a loss of coherence; (ii) as the trajectories do not follow the full length in the oscillatory radius r_{osc} , the electron cannot acquire in full extent the corresponding (pon-

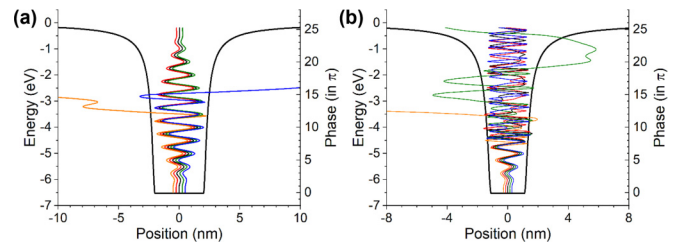


FIG. 11. Dynamics of selected trajectories with zero initial velocity and different initial positions within the well for (a) 4 nm diameter dots and (b) 2 nm diameter dots. The phase of the laser field oscillations is defined as $\varphi = \omega t/\pi$ where ω is the laser frequency. The trajectories leaving the well correspond to particles stochastically heated to energies above the work function V_0 .

deromotive) energy. To verify this, we calculated the kinetic energy of each trajectory within the time window when the electron is moving in the region where in our model harmonic emission would occur (near the walls); we define this region as the interval from the dot's radius until the point where the gradient of the potential drops to 1% from its maximum value $\frac{2}{3\sqrt{3}} |V_0/q|$ located at the points $|x| = \frac{d}{2} + |\frac{q}{\sqrt{2}V_0}|$. The results of calculations are shown in Fig. 12. Two important conclusions follow from the analysis of Fig. 12. First, there is a clear reduction in the maximum kinetic energy acquired by electrons for dots with a diameter $d < 3$ nm for both driving laser wavelengths. This reduction is larger for the longer wavelength λ , in agreement with the TDSE simulations and the simple classical considerations, i.e., when $d < r_{\text{osc}}$. Second, there is clear chaotization of the electron trajectories' dynamics caused by the scattering off the wall. Without the scattering, all electron trajectories would show regular oscillations with half of the optical cycle periodicity (compared to Fig. 11), reflected in regular oscillations in the kinetic energy (can be seen in Fig. 12 for relatively low energies). The scattering leads to a dephasing between the trajectories and washing out of regular oscillation structure in the kinetic energy (for energies roughly above 4 eV in Fig. 12).

Thus, the trajectory analysis suggests that the origin of the suppression in harmonic yield for highest harmonic orders in small dots is caused by two contributions: (i) the small dot sizes prevent full oscillatory dynamics of the electron inside the dot, leading to a reduced acquisition of kinetic energy and, thus, prohibits emission of the highest harmonics; (ii) the scattering off the dot's wall leads to a chaotization of the dynamics, which corresponds to dephasing and decoherence in the quantum description, and causes an additional suppression of emission of the highest harmonic orders. These effects become important when the dot size d is less than the oscillatory radius r_{osc} of electron motion, thus explaining the experimentally observed scaling with the driving wavelength and intensity.

Finally, we tried to reproduce in the frame of the particle-in-a-box model the increased nonlinearity in the intensity scaling of harmonics. For this we introduced a position-dependent effective mass of electron, such that at the interface the electron's effective mass changes from that of the bulk (for wurtzite CdSe $m_{\text{eff}} = 0.13 m_0$) to that of free space m_0 . Also, we included the effect of the optical field enhancement,

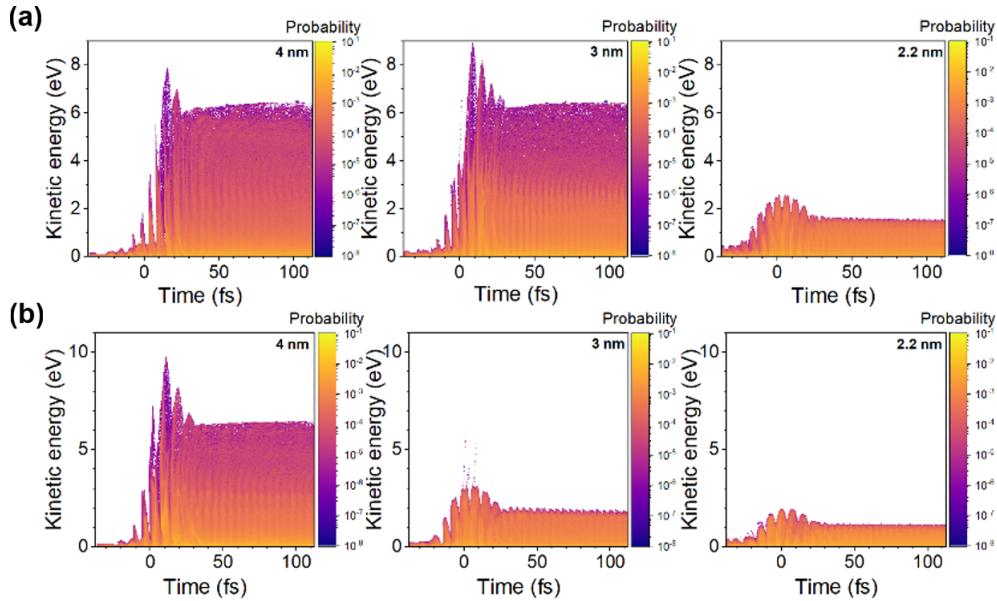


FIG. 12. Kinetic energy at different electron trajectories, moving at a given moment of time within the emission region, for different dot diameters and driven by (a) 3.75 μm and (b) 4.75 μm laser wavelength.

which leads to an increase in the field amplitude outside the QD up to factor of 2.2. Both effects cause an abrupt change of acceleration and consequently an increase of HHG resulting in a stronger power dependence as soon as the optical field forces the electron to leave the QD. However, we were not able to reproduce the increase in the power index for the fifth harmonic up to the value 6.7, retrieved from the experimental data.

As stated above, this very simple particle-in-a box model cannot describe the coherent electron-hole dynamics in the conduction and valence bands giving rise to the emission of harmonics larger than the band gap. However, this interband recombination mechanism of HHG is very sensitive to dephasing of the electron-hole motion. Scattering of the electron wave packet off the dot's boundary will ultimately lead to a dephasing of the electron-hole motion and a momentum mismatch. Therefore, we can expect that this dephasing of the electron-hole motion, induced by the off-wall scattering, will also lead to a significant drop in the efficiency of HHG above the band gap.

V. CONCLUSIONS

In conclusion, we experimentally investigated the confinement sensitivity of HHG in layers of semiconductor quantum dots as a function of dot diameter, laser intensity, polarization, and wavelength. We have shown that a reduction in size of quantum dots d below the oscillatory radius r_{osc} of the electron wave packet motion results in strong suppression of highest-order harmonics with energies of quanta above the band gap. Since these harmonics are predominantly generated by the electron-hole recombination mechanism, an analog of Corkum's three-step HHG mechanism in gases [30,31], we suggest that this suppression is due to inefficient acceleration of the electron wave packet, spatially confined within dots. Numerical simulations, based on rtTDDFT, and a simple

quantum dynamical model TDSE for a particle in a box, confirm the strong suppression of harmonic emission. An accompanying classical trajectory analysis, based on Monte Carlo simulations, clearly shows that for dots with a diameter $d < r_{\text{osc}}$, trajectories bounce off the dot's walls, leading to (i) a substantial reduction of acquired ponderomotive energy and (ii) a chaotization and randomization of motion, leading to a loss of coherence. These two effects are responsible for the observed suppression of the highest-order harmonics. We believe that our experimental results demonstrate a regime of extreme nonlinear optics in nanoscale solids, an intermediate between the bulk solid behavior and single-molecule response. They mark a border set by strong quantum confinement in minimum size of nanostructuring in solids, that is crucial for the development of nanophotonic elements, and metasurface and topological insulator structures for control and enhancement of HHG efficiency [32–34].

ACKNOWLEDGMENTS

C.H., M.T., V.K., R.B., F.Y., D.K., M.W., S.G., and U.P. gratefully acknowledge financial support by the German Research Foundation DFG under Collaborative Research Center SFB 1375 “NOA”, Projects No. A1 and No. C4. S.G. and M.R. gratefully acknowledge financial support by ERC within Consolidator Grant “QUEM-CHEM.” M.R., C.H., and A.C. gratefully acknowledge the Supercomputer Cluster PC2 in Paderborn for granting the calculation time. D.K., M.W., and C.R. gratefully acknowledge financial support by the State of Thuringia within ProExcellence Initiative Abbe Center of Photonics (ACP) 2020. M.W. gratefully acknowledges financial support by Fonds der Chemischen Industrie (FCI). A.B. and A.P. gratefully acknowledge financial support by the Austrian Science Fund (FWF) under Project No. I 4566. C.S. and M.Z. gratefully acknowledge financial support by the Federal Ministry of Education and Research (BMBF) under

“Make Our Planet Great Again–German Research Initiative” (Grant No. 57427209 “QUESTforENERGY”) implemented by DAAD. A.U. gratefully acknowledges financial support by the German Research Foundation within the infrastructure Grant No. 390918228–INST 275/391-1. The authors thank Dr. Marco Diegel for performing XRD measurements, Professor Misha Ivanov for fruitful discussions, and Dr. I. Gonoskov for discussions about 1D-TDSE dot calculations.

APPENDIX: SAMPLE PRODUCTION AND CHARACTERIZATION

1. Chemicals

Triethylphosphine oxide (TOPO, 99%), triethylphosphine (TOP, 97%), cadmium oxide (CdO, 99.99%), selenium (Se, 99.99%), toluene (99.8% anhydrous), and methanol (99.8% anhydrous) were purchased from Sigma-Aldrich and octadecylphosphonic acid (ODPA, 97%) was purchased from Carl Roth.

2. Synthesis of colloidal CdSe quantum dots

Colloidal CdSe quantum dots were prepared via hot injection as described in [13]. In a 25 ml three-neck flask with a

magnetic stirrer inside, 60 mg CdO, 0.28 g ODPA, and 3 g TOPO were mixed, heated up to 150 °C, and evacuated for 1 h. Then, under nitrogen flow the solution was heated up; it turned clear and colorless at 310 °C. At this point 1.5 g TOP was injected into the flask and the solution was allowed to heat up again. A TOP:Se solution (0.058 g TOP + 0.36 g Se) was injected into the solution while varying the injection temperature, and the growth time was chosen according to the desired size of the quantum dot. A diameter of 2.2 nm was achieved by injecting the TOP:Se solution at 330 °C and cooling down the solution by immediately removing the heating mantle and using cold water around the flask for faster cooling. Larger particles of sizes 4.4, 6, and 8 nm diameter were achieved by injecting the TOP:Se solution at 320 °C and extending the growth period to 1.5 min, 5 min, and 1 h, respectively, at 300 °C followed by cooling down the flask. When the temperature was around 80 °C, 10 ml of toluene was injected. After the synthesis, the particles were cleaned by precipitation with MeOH and centrifugation at 5300 rpm for 10 min, followed by discarding the supernatant and redispersing the QD solid in 10 ml toluene. The cleaning procedure was performed four times in total. The final product was dispersed in 10 ml toluene and stored under inert atmosphere.

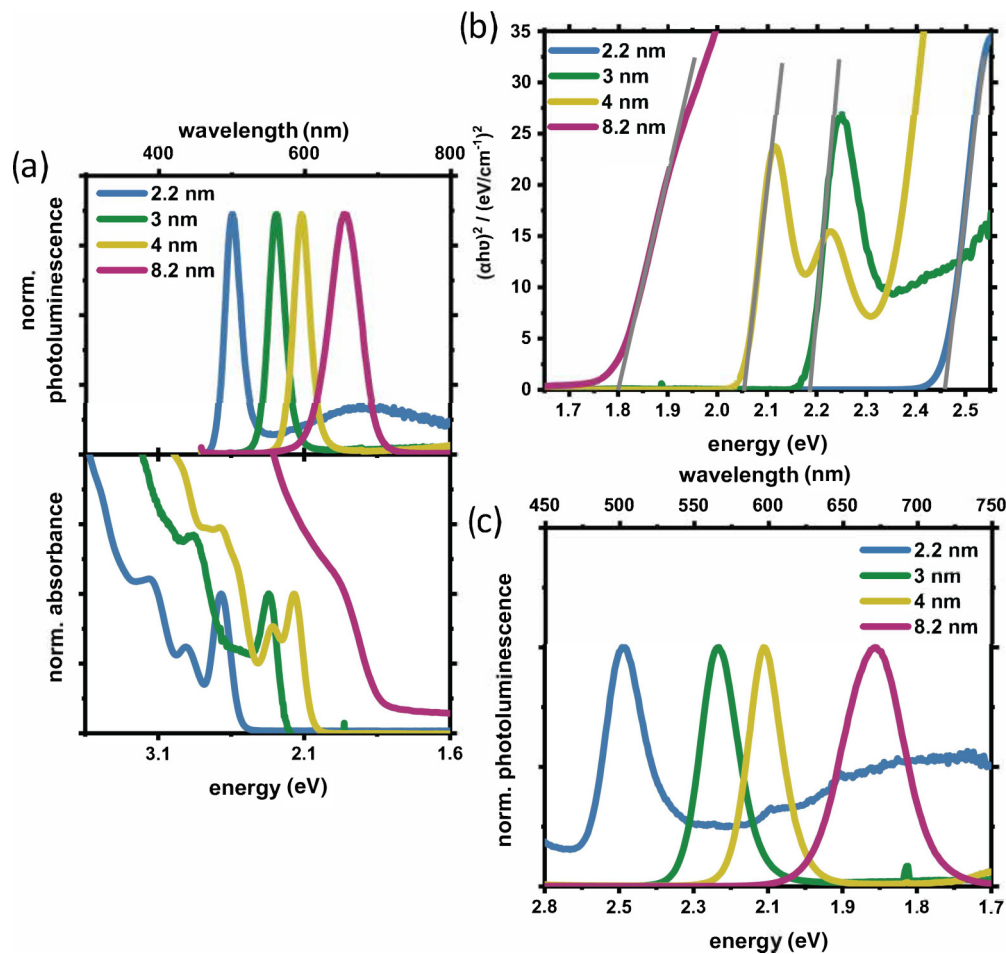


FIG. 13. (a) UV/vis absorption (bottom panel) and normalized photoluminescence spectra (top panel) of CdSe QDs of different sizes used in this investigation dispersed in toluene. (b) Tauc plots for different sizes of CdSe QDs derived from absorption spectra of particles dispersed in toluene and (c) normalized photoluminescence spectra of different sizes of CdSe QDs deposited in the layer.

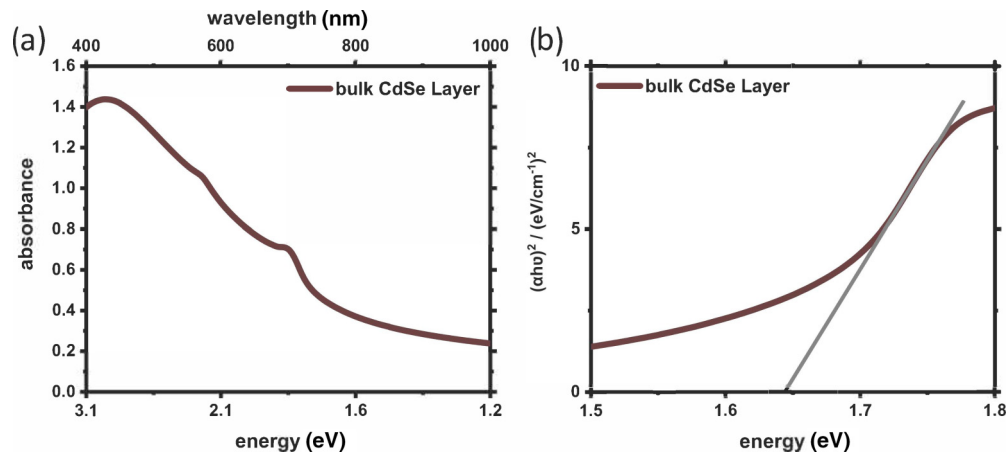


FIG. 14. (a) UV/vis absorption spectra and (b) Tauc plot of the bulk CdSe layer.

3. Deposition of colloidal quantum dots into layers

Prior to deposition of colloidal QDs, $1\text{ cm} \times 1\text{ cm}$ sapphire substrates (purchased from CrysTec) were cleaned with acetone, methanol, Hellmanex, and water with 20 min ultrasonication each followed by air drying. Then 200 μl each of 2.2 nm QD (0.44 mM), 3 nm QD (0.025 mM), 4 nm QD (6.8 μm), and 8.2 nm QD (2.8 μm) solution (in toluene) were drop casted and finally dried under vacuum.

4. Preparation of bulk CdSe layer

The bulk CdSe layer was prepared via chemical bath deposition as reported in [18]. In the first step Na_2SeSO_3 was prepared. Therefore, in a 25 ml three-neck round-bottom flask, 110 mg of Se and 40 mg of Na_2SO_3 were mixed followed by an addition of 7 ml of distilled water and stirred for 24 h at 90°C . Sapphire substrates were cleaned with acetone and isopropanol for 20 min in an ultrasonic bath followed by drying by air blowing. In the second step, in a 25 ml two-neck round-bottom flask with a magnetic stirrer inside, 620 mg of cadmium acetate hydrate was mixed with 5 ml of distilled water and stirred. Then 292 mg of ethylenediaminetetraacetic acid (EDTA) dissolved in 4 ml of ammonia was added. The pH of the solution was adjusted to 10–11 by addition of more NH_3 . The cleaned sapphire substrate was placed inside the flask with a holder, from the top, and the solution was heated to 90°C followed by the addition of 5 ml of Na_2SeSO_3 . The color of the solution was observed to turn into yellow, then orange, and finally red. Then the solution was stirred for 1 h more at 90°C . Finally, the solution was removed, and the substrates were washed with distilled water in a Petri dish. In the third step, the substrates were then taken for annealing for 4 h at 600°C under nitrogen flow to convert the original zinc-blende phase to the wurtzite phase.

5. TEM

Colloidal QDs were deposited on a carbon-coated Cu grid (purchased from Plano GmbH) followed by vacuum drying. Transmission electron microscopy (TEM) images were recorded in conventional (TEM) and scanning mode (STEM) using a JEM-ARM200F NEOARM (Jeol) operating at

80 kV, equipped with a spherical aberration corrector, bright-field (BF), annular bright-field (ABF), and annular dark-field (ADF) detectors. Images were processed using the IMAGEJ 1.53A program [35]. Size and size distribution were evaluated using 500–1000 particles for each QD batch.

6. SEM

Scanning electron microscopy images were collected of the layers deposited on a silicon wafer using a dual-beam Helios NanoLab G3 UC (FEI).

7. AFM

A Bruker Dimension Edge was used in tapping mode to collect the micrographs. To determine film thickness, a scratch was made on the layer and AFM micrographs were collected crossing the scratch.

8. X-ray diffraction analysis (XRD)

Grazing incidence x-ray diffraction (GIXRD) was performed using a Panalytical X'Pert Pro MPD ($\text{Cu } K\alpha_{1,2}$) with omega angle 0.4° – 3° . XRD analysis was performed for the

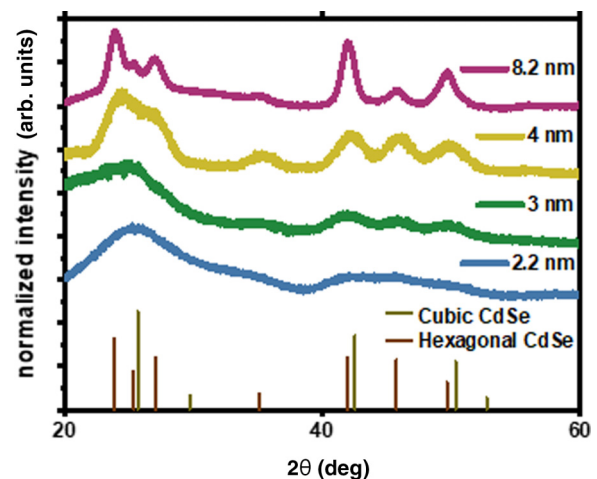


FIG. 15. XRD patterns of CdSe QDs of different sizes.

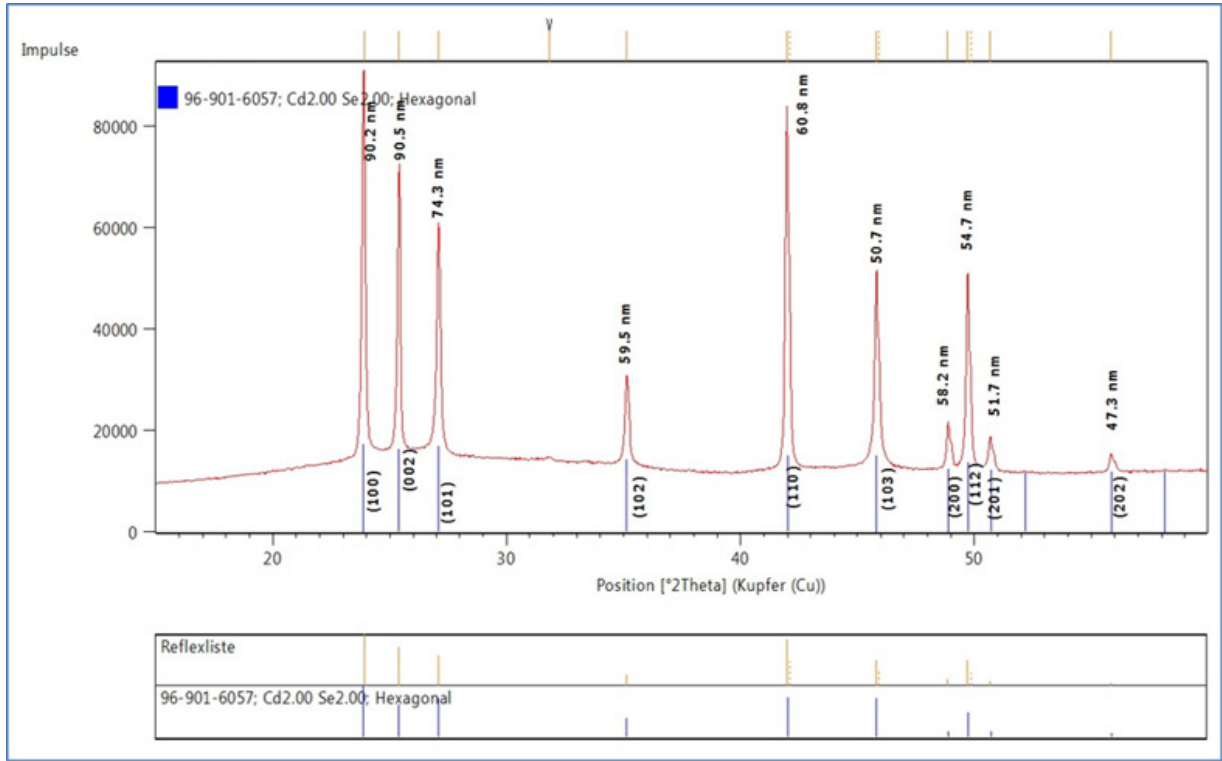


FIG. 16. XRD of bulk CdSe layer.

bulk CdSe layer and the CdSe QDs. For this, colloidal QDs were deposited on glass substrates via drop casting.

9. Steady-state UV/Vis absorption spectroscopy

UV/Vis absorption spectra were recorded using a JASCO V780 UV-visible/NIR spectrometer for QDs dispersed in toluene (3 ml) in a quartz cuvette with 1 cm path length. Similarly, UV/vis absorption spectra of solid layers were recorded using a sample holder suitable for 1 cm × 1 cm layers. Absorption spectra of the bulk CdSe layer (deposited on sapphire) were recorded using a clean sapphire substrate as reference.

10. Photoluminescence spectroscopy

Photoluminescence spectra of the quantum dots dispersed in toluene were collected by exciting at 3.1 eV (400 nm) using a FLS980 photoluminescence spectrometer (Edinburgh Instruments Ltd, Livingston, UK). Absolute photoluminescence yield Φ_{PL} determination was performed in an integrating

sphere set up with a 1 cm path length quartz cuvette filled with QDs dispersed in toluene with around 0.1 optical density. Photoluminescence spectra of the quantum dot layers were collected by exciting at 3.1 eV (400 nm) using a Horiba Scientific Fluorolog-3 spectrofluorometer. Spectra collection was done in the so-called front face mode, placing the front face of the sample at 22.5° to the excitation beam.

11. Optical properties of QDs

In the absorption spectra of the quantum dots, characteristic electronic transitions are observed which can be assigned to the lowest band edge $1S_e-2S_{3/2(h)}$ and to the higher energy $1P_e-1P_{3/2(h)}$ transitions. With increasing size, the position of the first excitonic peak is redshifted (Fig. 13). The diameter of the QDs was estimated from the spectral position of first excitonic transition in the absorption spectra by the method described in [16] and compared to results from TEM images. The results from both methods are in good agreement; deviations for the largest particles are caused by a slight anisotropy

TABLE II. Sizes, spectral characteristics, quantum yields of the photoluminescence Φ_{PL} , and band gaps of different CdSe QDs presented as different colors as in Fig. 1.

Size (absorption spectra) (nm)	First absorption peak (eV)	Band edge photoluminescence peak (eV)	Band gap (E_g) (eV) (Tauc plot)	Φ_{PL} (%)	Size (absorption spectra) (nm)
2.2	2.55	2.48	2.48 ± 0.05	11 ± 2	2.2
3	2.25	2.21	2.18 ± 0.07	2.6 ± 2	3
4	2.11	2.08	2.05 ± 0.06	1.5 ± 2	4
8.2	1.9	1.89	1.89 ± 0.02	0.3 ± 2	8.2

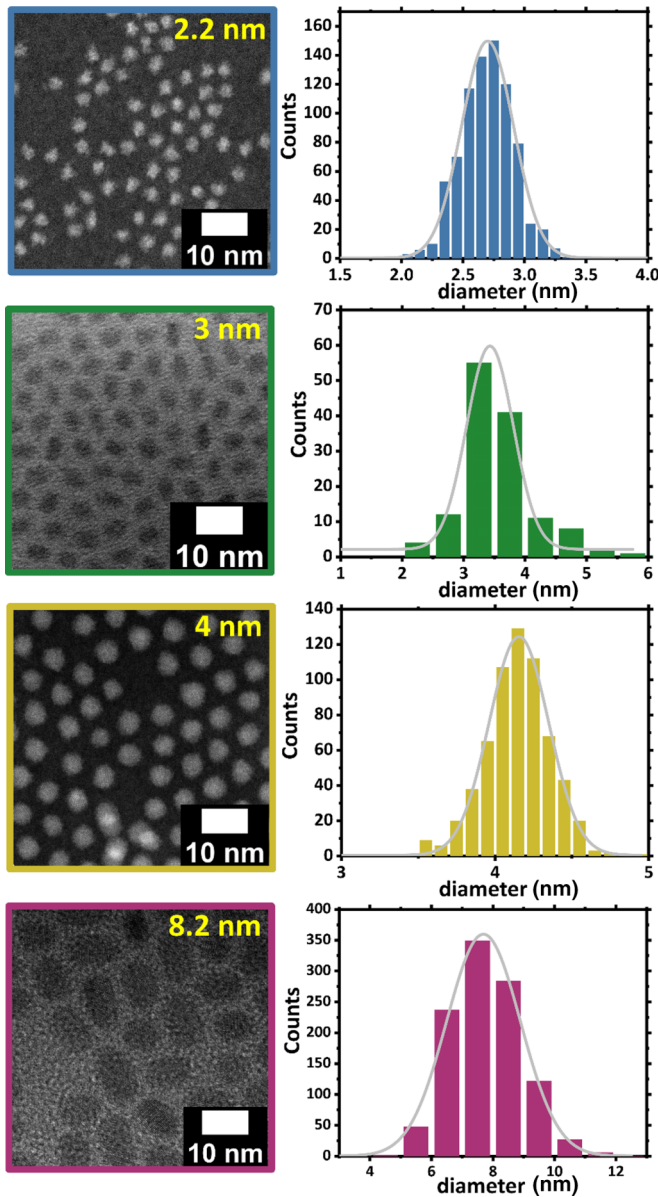


FIG. 17. TEM images and size distribution of different sizes of CdSe QDs shown by blue, green, yellow, and red (border of the images and histograms).

of the particles and the uncertainty of the exact peak position due to broad spectral features. Similar to the peak position in absorption spectra, the band edge luminescence peak is redshifted with increasing QD size. Additionally, for

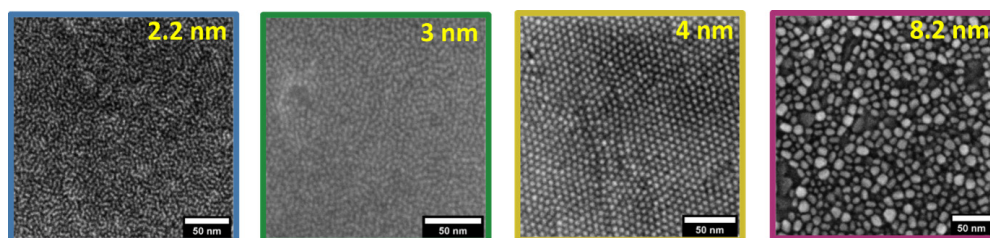


FIG. 18. SEM images of CdSe QDs of sizes 2.2 nm (blue), 3 nm (green), 4 nm (yellow), and 8.2 nm (red). The 2 and 3 nm sized QDs are below or just at the limit of the resolution of the instrument.

TABLE III. Size, size distribution, and aspect ratio of different sizes of CdSe QDs calculated from the TEM images in Fig. 17.

Size (absorption spectra) (nm)	Size (TEM) (nm)	FWHM (nm)	Aspect ratio
2.2	2.6	0.5	–
3	3.4	0.89	–
4	4.2	0.38	–
8.2	7.7	2.82	1.7:1

the smallest particles a broad emission band at wavelengths longer than 600 nm is observed originating from trap state emission (Fig. 13). Surface trap state emission appears more pronounced in smaller QDs due to a higher surface to volume ratio as compared to larger QDs. The quantum yield of the band edge luminescence decreases with increasing particle size in accordance with a report in the literature [36].

The band gap (E_g) of QDs with different sizes was derived from their absorption spectra via Tauc plots and compared to the position of the band edge photoluminescence band position (Fig. 14). The results from both methods show good agreement (Table II).

12. XRD—quantum dots

The XRD pattern in Fig. 15 corresponds to pure wurtzite CdSe with the characteristic reflection from (010), (011), (110), (013), and (112) at 23.93°, 25.38°, 42.0°, 45.84°, and 49.74° (ICSD: 60630). As an indication of smaller particles, relatively broad XRD peaks were observed for small quantum dots.

13. XRD—bulk sample

The XRD of the bulk CdSe layer is shown in Fig. 16 and clearly shows that the sample has the wurtzite phase. The hkl indices match very well the reference data for hexagonal wurtzite CdSe. From the fact that we see all the tabulated diffraction peaks and the intensity distribution correlate with the structure factor, we must expect no strong preferred crystal orientation. From the FWHM of the reflexes the crystallite size was determined using the Scherrer formula (HIGHSCORE+ program) showing that the layer consists of crystallites with sizes on the order of 50 nm. The diffraction profiles are quite narrow and homogeneous. There is no indication of much difference in the crystallite sizes. Further, one can expect no strong crystallite defects which would affect the symmetry of the profiles.

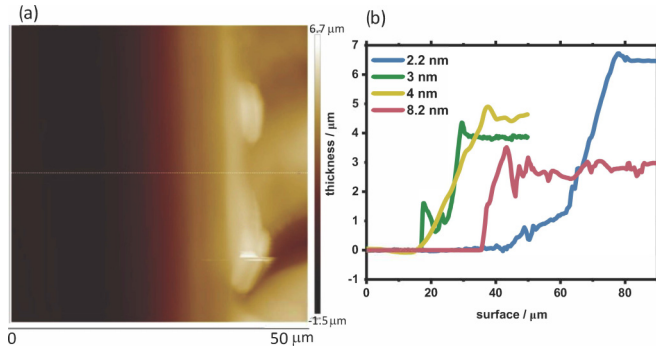


FIG. 19. (a) AFM image of 4 nm QD. (b) Thickness determination curve of the QD layers, where thickness is calculated from the bottom of the scratch (at 0) to the top of the surface.

14. Transmission electron microscopy (TEM)

TEM images were used to determine the average sizes and size distribution of QDs as depicted in Fig. 17 and Table III. The aspect ratio of the particle which is not perfectly spherical was also determined.

15. Scanning electron microscopy (SEM)

Scanning electron microscopy images were collected of the layers deposited in a silicon wafer using a dual-beam Helios

TABLE IV. Thickness of the CdSe QD and bulk CdSe layers determined from atomic force micrographs.

Size (absorption spectra) (nm)	Thickness (μm)
2.2	6.4 ± 0.1
3	3.8 ± 0.1
4	4.5 ± 0.12
8.2	2.8 ± 0.24
Bulk CdSe	0.140 ± 0.012

NanoLab G3 UC (FEI). As shown in Fig. 18, an organized array of quantum dots was observed. Although SEM images were collected in similar imaging conditions, due to different amounts of organic residuals left on the QD batches, there are differences in the contrast and image quality.

16. Atomic force microscopy (AFM)

The atomic force microscopy technique was used to determine the thickness of the layers of both bulk and quantum dots as depicted in Fig. 19 and Table IV. For this a scratch was made on the QD layer and AFM micrographs were collected over the scratch. The thickness was determined from the thin film surface to the bottom of the scratch as shown in Fig. 19(b). A mean value was determined in both the surface and bottom scratch region of the graph [Fig. 19(b)] and subtracted to determine the thickness.

- [1] D. Golde, T. Meier, and S. W. Koch, High harmonics generated in semiconductor nanostructures by the coupled dynamics of optical inter- and intraband excitations, *Phys. Rev. B* **77**, 075330 (2008).
- [2] S. Ghimire, A. D. DiChiara, E. Sistrunk, P. Agostini, L. F. DiMauro, and D. A. Reis, Observation of high-order harmonic generation in a bulk crystal, *Nat. Phys.* **7**, 138 (2011).
- [3] Y. S. You, D. A. Reis, and S. Ghimire, Anisotropic high-harmonic generation in bulk crystals, *Nat. Phys.* **13**, 345 (2017).
- [4] M. R. Bionta, E. Haddad, A. Leblanc, V. Gruson, P. Lassonde, H. Ibrahim, J. Chaillou, N. Émond, M. R. Otto, A. Jiménez-Galán, R. E. F. Silva, M. Ivanov, B. J. Siwick, M. Chaker, and F. Légaré, Tracking ultrafast solid-state dynamics using high harmonic spectroscopy, *Phys. Rev. Res.* **3**, 023250 (2021).
- [5] G. Vampa, T. J. Hammond, N. Thiré, B. E. Schmidt, F. Légaré, C. R. McDonald, T. Brabec, D. D. Klug, and P. B. Corkum, All-Optical Reconstruction of Crystal Band Structure, *Phys. Rev. Lett.* **115**, 193603 (2015).
- [6] A. A. Lanin, E. A. Stepanov, A. B. Fedotov, and A. M. Zheltikov, Mapping the electron band structure by intraband high-harmonic generation in solids, *Optica* **4**, 516 (2017).
- [7] N. Tancogne-Dejean, O. D. Mücke, F. X. Kärtner, and A. Rubio, Impact of Electronic Band Structure in High-Harmonic Generation Spectra of Solids, *Phys. Rev. Lett.* **118**, 087403 (2017).
- [8] J. Park, A. Subramani, S. Kim, and M. F. Ciappina, Recent trends in high-order harmonic generation in solids, *Adv. Phys.: X* **7**, 2003244 (2022).
- [9] H. Lakhota, H. Y. Kim, M. Zhan, S. Hu, S. Meng, and E. Goulielmakis, Laser picoscopy of valence electrons in solids, *Nature (London)* **583**, 55 (2020).
- [10] G. Vampa and T. Brabec, Merge of high harmonic generation from gases and solids and its implications for attosecond science, *J. Phys. B* **50**, 083001 (2017).
- [11] K. Nakagawa, H. Hirori, S. A. Sato, H. Tahara, F. Sekiguchi, G. Yumoto, M. Saruyama, R. Sato, T. Teranishi, and Y. Kanemitsu, Size-controlled quantum dots reveal the impact of intraband transitions on high-order harmonic generation in solids, *Nat. Phys.* **18**, 874 (2022).
- [12] L. Carbone, C. Nobile, M. De Giorgi, F. Della Sala, G. Morello, P. Pompa, M. Hytch, E. Snoeck, A. Fiore, I. R. Franchini, M. Nadasan, A. F. Silvestre, L. Chiodo, S. Kudara, R. Cingolani, R. Krahné, and L. Manna, Synthesis and micrometer-scale assembly of colloidal CdSe/CdS nanorods prepared by a seeded growth approach, *Nano Lett.* **7**, 2942 (2007).
- [13] A. Schleusener, M. Micheel, S. Benndorf, M. Rettenmayr, W. Weigand, and M. Wächtler, Ultrafast electron transfer from CdSe quantum dots to an [FeFe]-hydrogenase mimic, *J. Phys. Chem. Lett.* **12**, 4385 (2021).
- [14] R. Koole, E. Gröneveld, D. Vanmaekelbergh, A. Meijerink, and C. de Mello Donegá, *Size effects on semiconductor nanoparticles*, in *Nanoparticles*, edited by C. de Mello Donegá (Springer, Berlin, 2014).
- [15] A. L. Abdelhady, M. Afzaal, M. Azad Malik, and P. O'Brien, Flow reactor synthesis of CdSe, CdS, CdSe/CdS, and CdSeS

- nanoparticles from single molecular precursor(s), *Mater. Chem.* **21**, 18768 (2011).
- [16] W. W. Yu, L. Qu, W. Guo, and X. Peng, Experimental determination of the extinction coefficient of CdTe, CdSe, and CdS nanocrystals, *Chem. Mater.* **15**, 2854 (2003).
- [17] A. I. Ekimov, F. Hache, M. C. Schanne-Klein, D. Ricard, C. Flytzanis, I. A. Kudryavtsev, T. V. Yazeva, A. V. Rodina, and Al. L. Efros, Absorption and intensity-dependent photoluminescence measurements on CdSe quantum dots: Assignment of the first electronic transitions, *J. Opt. Soc. Am. B* **10**, 100 (1993).
- [18] T. S. Shyju, S. Anandhi, R. Indirajith, and R. Gopalakrishnan, Effects of annealing on cadmium selenide nanocrystalline thin films prepared by chemical bath deposition, *J. Alloys Compd.* **506**, 892 (2010).
- [19] N. Tancogne-Dejean, O. D. Mücke, F. X. Kärtner, and A. Rubio, Ellipticity dependence of high-harmonic generation in solids originating from coupled intraband and interband dynamics, *Nat. Commun.* **8**, 745 (2017).
- [20] S. Grimme, C. Bannwarth, and P. Shushkov, A robust and accurate tight-binding quantum chemical method for structures, vibrational frequencies, and noncovalent interactions of large molecular systems parametrized for all *spd*-block elements ($Z = 1-86$), *ACS J. Chem. Theory Comput.* **13**, 1989 (2017).
- [21] N. Tancogne-Dejean, M. J. T. Oliveira, X. Andrade, H. Appel, C. H. Borca, G. Le Breton, F. Buchholz, A. Castro, S. Corni, A. A. Correa, U. De Giovannini, A. Delgado, F. G. Eich, J. Flick, G. Gil, A. Gomez, N. Helbig, H. Hübener, R. Jestädt, J. Jornet-Somoza *et al.*, OCTOPUS, a computational framework for exploring light-driven phenomena and quantum dynamics in extended and finite systems, *J. Chem. Phys.* **152**, 124119 (2020).
- [22] J. P. Perdew and A. Zunger, Self-interaction correction to density-functional approximations for many-electron systems, *Phys. Rev. B* **23**, 5048 (1981).
- [23] C. Hartwigsen, S. Goedecker, and J. Hutter, Relativistic separable dual-space Gaussian pseudopotentials from H to Rn, *Phys. Rev. B* **58**, 3641 (1998).
- [24] <https://materialsproject.org/materials/mp-1070>.
- [25] N. Tancogne-Dejean (private communication).
- [26] I. Floss, C. Lemell, G. Wachter, V. Smejkal, S. A. Sato, X.-M. Tong, K. Yabana, and J. Burgdörfer, *Ab initio* multiscale simulation of high-order harmonic generation in solids, *Phys. Rev. A* **97**, 011401(R) (2018).
- [27] N. J. Shevchik, J. Tejada, M. Cardona, and D. W. Langer, Photoemission and density of valence states of II-VI compounds: ZnTe, CdSe, CdTe, HgSe and HgTe, *Phys. Status Solidi B* **59**, 87 (1973).
- [28] L. Lehtovaara, J. Toivanen, and J. Eloranta, Solution of time-independent Schrödinger equation by the imaginary time propagation method, *J. Comput. Phys.* **221**, 148 (2007).
- [29] J. D. Jackson, *Classical Electrodynamics*, 3rd ed. (John Wiley & Sons, Inc., New York, 1998).
- [30] P. B. Corkum, Plasma Perspective on Strong Field Multiphoton Ionization, *Phys. Rev. Lett.* **71**, 1994 (1993).
- [31] G. Vampa, C. McDonald, A. Fraser, and T. Brabec, High-harmonic generation in solids: Bridging the gap between attosecond science and condensed matter physics, *IEEE J. Sel. Top. Quantum Electron.* **21**, 8700110 (2015).
- [32] G. Vampa, B. Ghamsari, S. S. Mousavi, T. Hammond, A. Olivieri, E. Lisicka-Skrek, A. Y. Naumov, D. Villeneuve, A. Staudte, P. Berini, and P. Corkum, Plasmon-enhanced high-harmonic generation from silicon, *Nat. Phys.* **13**, 659 (2017).
- [33] G. Siroki, P. D. Haynes, D. K. K. Lee, and V. Giannini, Protection of surface states in topological nanoparticles, *Phys. Rev. Mater.* **1**, 024201 (2017).
- [34] G. Zograf, K. I. Koshelev, A. Zalogina, V. Korolev, R. Hollinger, D.-Y. Choi, M. Zuerch, C. Spielmann, B. Luther-Davies, D. Kartashov, S. V. Makarov, S. S. Kruk, and Y. Kivshar, High-harmonic generation from resonant dielectric metasurfaces empowered by bound states in the continuum, *ACS Photonics* **9**, 567 (2022).
- [35] J. Schindelin, I. Arganda-Carreras, E. Frise, V. Kaynig, M. Longair, T. Pietzsch, S. Preibisch, C. Rueden, S. Saalfeld, B. Schmid, J.-Y. Tinevez, D. J. White, V. Hartenstein, K. Eliceiri, P. Tomancak, and A. Cardona, FIJI: An open-source platform for biological-image analysis, *Nat. Methods* **9**, 676 (2012).
- [36] J. Zhang, X. Zhang, and J. Y. Zhang, Size-dependent time-resolved photoluminescence of colloidal CdSe nanocrystals, *J. Phys. Chem. C* **113**, 9512 (2009).
- Correction:* The previously published Figure 2 was not the final version of the figure and has been replaced.